

Impacts of nanopore structure and elastic properties on stress-dependent permeability of gas shales

Rui Zhang ^{a, b, *}, Zhengfu Ning ^{a, b}, Feng Yang ^{a, b}, Xin Wang ^c, Huawei Zhao ^{a, b}, Qing Wang ^{a, b}

^a State Key Laboratory of Petroleum Resources and Prospecting, China University of Petroleum, Beijing, China

^b Key Laboratory of Petroleum Engineering of the Ministry of Education, China University of Petroleum, Beijing, China

^c Research Institute of Petroleum Exploration & Development, PetroChina, Beijing, China

ARTICLE INFO

Article history:

Received 10 October 2014

Received in revised form

31 December 2014

Accepted 2 February 2015

Available online 7 February 2015

Keywords:

Gas shales

Pore structure

Stress-dependent porosity and permeability

Mechanical property

ABSTRACT

This paper presented the stress-dependent porosity and permeability measurements of shale in lower Silurian Longmaxi Formation using a PoroPDP-200 Pulse decay permeameter. The pore structure was investigated by mercury injection and nitrogen adsorption measurements. Micron-sized fractures and nanopore structure of shale samples were identified through mercury saturation curves and adsorption–desorption isotherms. Uniaxial and triaxial tests were conducted so as to measure the elastic parameters of the shale samples. Three analytical models of pore compressibility were displayed to investigate the effects of pore geometry and rock elastic properties on pore compressibility. Pulse-decay permeability measurements revealed that an exponential function could describe the permeability deterioration upon applied effective stress. The stress-dependent permeability of shale was more sensitive than sandstone because of the high pore compressibility. It could be observed from analytical models that pore compressibility increased with a decreasing pore aspect ratio and Young's modulus. Microfractures were identified by the shape of mercury capillary pressure curves. The nanopores of the shale samples were dominated by a slit-shaped geometry (low aspect ratio), which was observed by hysteresis loop of nitrogen adsorption analysis (Type H3). Uniaxial and triaxial tests results showed that static Young's modulus of shale samples were sensitive to total organic carbon (TOC) and montmorillonite-illite mixed layer content. Pore compressibility was sensitive to the aspect ratio, yet insensitive to Young's modulus above 20 GPa. When the Young's modulus was less than 20 GPa, pore compressibility was both sensitive to aspect ratio and Young's modulus. The stress-dependent permeability data of samples with micron-sized fractures could also be fitted to the Walsh model, which showed that the permeability of microfractures in shale samples were more sensitive to effective stress than hydraulic fractures because of the fracture scale. These results showed that reservoir engineers could accurately predict the stress-dependent permeability in shale, and estimate the gas flow properties in macro-scale and micro-scale pores and fractures.

© 2015 Elsevier B.V. All rights reserved.

1. Introduction

Shale porosity, permeability, and their relations under effective stress are crucial for gas flow. Consequently, the change of porosity and permeability under stress would have a significant influence on shale gas performance. Precisely predicting the stress-dependent permeability of shale formation is challenging because the lack of

information on stress-induced permeability-porosity at micro-scale. Many empirical relationships including logarithmic, power law and polynomial functions have been used in different types of rocks. Jones (1975) used a logarithmic empirical relationship to describe fractured carbonates permeability with respect to effective stress, Walsh (1981) represented the theoretical derivation procedure of this logarithmic relationship by using Poiseuille's equation of fracture system. Gangi (1978) derived polynomial relationships to describe permeability with confining pressure of whole and fractured porous rock. Dong et al. (2010) suggest that permeability of sandstones and silty-shales with confining stress

* Corresponding author. State Key Laboratory of Petroleum Resources and Prospecting, China University of Petroleum, Beijing, China.

E-mail address: vvvbst2005@163.com (R. Zhang).

follow a power law relationship, rather than an exponential relationship. However, many investigations have shown that permeability-porosity relations with effective stress can be excellently described with an exponential relationship. [Mckee et al. \(1988\)](#) derived a fundamental exponential relationship to describe the permeability and porosity as a function of effective stress of coal and other tight formations, including shales. [Reyes et al. \(2002\)](#) obtained an exponential relationship between permeability and stress on shale samples in Oklahoma using a steady state method. [Chalmers et al. \(2012\)](#) and [Cho et al. \(2013\)](#) also employed an exponential relationship in Devonian and Bakken shales using a pulse decay method. [David et al. \(1994\)](#) defined a pressure sensitive coefficient and highlighted the larger pressure sensitivity mean a sharper permeability decrease; pore compressibility is proportional to pressure sensitive coefficient.

[Clarkson et al. \(2012\)](#) suggested that microfractures and slit-shaped pores cause stress sensitivity in shales, which also implies high pore compressibility causes permeability stress sensitivity.

In this paper, three analytical models of pore compressibility were used to investigate the effect of pore geometry and rock elastic properties on pore compressibility. Further, a series laboratory experiments were conducted to investigate pore structures and mechanical properties of shale samples. Mercury Injection Capillary Pressure (MICP) and nitrogen adsorption can quantitatively characterize pore aperture from macro-to micro-pores, and can be used to calculate pore size distribution (PSD) ([Curtis et al., 2010](#); [Clarkson et al., 2012](#); [Chalmers et al., 2012](#)). Micro-fractures can be identified by the shape of mercury capillary pressure

curve. The nanopore structure can be speculated by hysteresis loop of nitrogen adsorption analysis. Such interpretation of pore structure can be used to further characterize fractures at the macro- and micro-scale. In addition, the Young's moduli of shale samples were measured by uni- and tri-axial tests. The Young's modulus response to petrographic composition and confining pressure were elucidated. Finally, data fitting of samples with micron-to submicron-scale fractures using Walsh model were conducted in order to study the different fracture scale (natural and hydraulic fractures) on permeability stress sensitivity.

2. Samples and experiments

2.1. Description of samples

Samples are taken from black shales of Chang201-203 Well (2297–2386 m) and Wei 203 well (2539–2543 m) from within the lower Silurian Longmaxi Formation of Sichuan Basin, south China ([Fig. 1](#)). Longmaxi Formation is organic-rich with a bioclastic cherty black shale mixed with gray silty mudstones ([EIA, 2013, Fig. 2a](#)) that were deposited in a sedimentary shelf environment. High pyrite content reflects the anaerobic environment and strongly reducing action ([Fig. 2b](#)). We selected a total of eight samples from the two wells. A series of experiments were conducted so as to develop an insight into mineralogy and geochemistry via X-Ray diffraction (XRD), Rock-Eval, and field emission scanning electron microscope ([Table 1](#)).

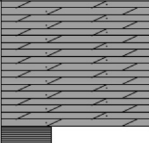
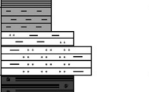
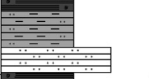

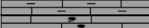


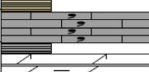

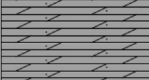
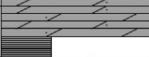
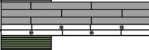

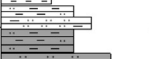

System	Epoch	Formation	Thickness	Section	Lithologic
SILURIAN	Middle-Lower	Hanjiadian	200–600		Gray sandy dolomite
	Lower	Shiniulan	150–350		Gray shale Mudstone Silty mudstone
		Longmaxi	100–400		Black siliceous shale Gray silty mudstone Siltstone
ORDOVICIAN	Upper	Wufeng	3–10		Black siliceous shale
		Dongcaogou	2–7		Gray marlstone
	Middle	Baota	20–60		Gray containing biological crumbs limestone
		shizipu	10–100		Gray containing biological crumbs limestone Argillaceous limestone
	Lower	Meitan	100–400		Gray shale, Silty shale Dark gray, Argillaceous limestone Kelly shale, Silty shale
		Honghuayuan	10–80		Gray containing biological crumbs limestone
CAMBRIAN	Upper	Loushanguan	550–650		Gray sandy dolomite
					Gray sandy dolomite Shale
	Lower	Qingxudong	100–200		Gray limestone Oolitic limestone
		Jindingshan	115–147		Grayish-green shale
		Mingxinsi	139–371		Grayish-green shale Mudstone, Silty mudstone
		Niutitang	125–481		Gray silty mudstone Siltstone Black siliceous shale

Fig. 1. Integrated histogram of Sichuan Basin from Cambrian to Silurian systems.

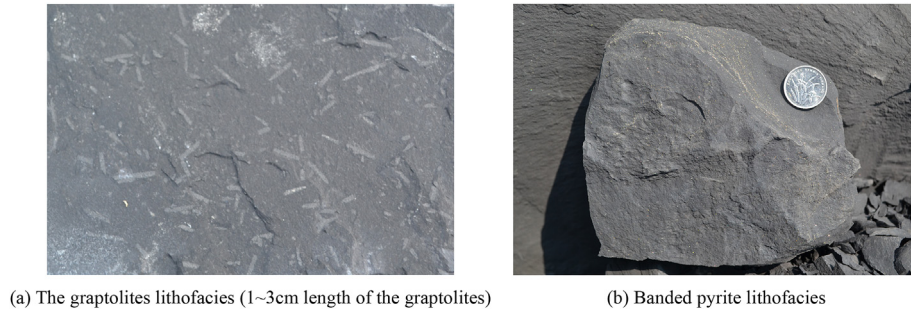


Fig. 2. The surface of the outcrop.

2.2. Stress-dependent permeability test

The initial permeability values of the shale samples ranged from 0.16 to 0.51 μD . A PoroPerm PDP-200 Pulse Permeameter was used to determine shale matrix permeability values under various confining pressures at a given pore pressure, the Permeameter uses a pulse decay measurement technique which can measure permeability ranging from 0.00001 to 10 mD. In this study, we set the confining pressure to increase from 7 to 32 MPa with a constant pore pressure 7 MPa. The effective stress can be determined using Equation (1),

$$p_{\text{eff}} = p_c - n_k p_p \quad (1)$$

where p_{eff} is the effective stress, p_c is the confining pressure, p_p is the pore pressure, n_k is the permeability effective stress coefficient. For linear elastic homogeneous porous media, n_k is slightly less than unity (Berryman, 1992). For sandstones and carbonates with two minerals, n_k is more than unity (Al-Wardy, 2004; Ghabezloo, 2009). Kwon et al. (2001) measured n_k of illite-rich shale and found n_k approximately equal to unity. In this paper, we assume that n_k is equal to 1, in order to simplify the calculation. Thus, the effective stress ranges from 0 to 25 MPa.

2.3. MICP and nitrogen adsorption

The pore structure of shale samples are investigated by mercury injection capillary pressure (MICP) and low-pressure nitrogen adsorption, which were conducted on MicromeriticsR Autopore IV 9500 Series and Quadrasorb™ SI Surface Area Analyzer and Pore Size Analyzer. Since the pressure of mercury was increased from 0.0069 to 200 MPa, the pore diameter was determined to be greater than 7.2 nm using Washburn (1921) Equation (2),

$$d = \frac{-4\sigma \cos \theta}{p} \quad (2)$$

where d is the pore diameter, σ is the surface tension for Hg (485 dyne/cm), θ is the contact angle (140°) and p is the applied pressure.

Powdered samples were dried for 24 h at 105°C and outgassed at 150°C before nitrogen adsorption experiments. Nitrogen was used as an adsorbent at -196°C under low pressure (<0.1 MPa), and nitrogen adsorption–desorption isotherms were obtained.

2.4. Uniaxial and triaxial test

The TAW-1000 servostress and hydraulic control system was used to test static elastic mechanical properties under increasing hydraulic confining pressure. Core plugs were covered by polyvinyl

chloride, which became soft when heated so as to be used for wrapping the core. The designed maximum confining pressure of triaxial chamber is 140 MPa; and can accommodate samples of $\Phi 25$ to 50 mm long. The maximum axial compression is 1500 kN, and axial strain measures ranging from 0 to 5 mm/mm, and circumferential strain measures ranging from 0 to 4 mm/mm. Confining pressure, axial load, displacement and strain signal data were collected by automatic data acquisition control system, TESTSTAR2.

3. Models for describing pore compressibility

Mckee et al. (1988) derived an exponential function to describe the stress-dependent permeability of coal and other tight formations. The exponential function is expressed as

$$k = k_0 e^{-\gamma p_{\text{eff}}} \quad (3)$$

Consequently, a high value of γ corresponds to severe stress sensitivity.

David et al. (1994) pointed out that the stress sensitive coefficient γ is the product of porosity sensitivity exponent α and the pore compressibility β .

$$\gamma = \alpha \beta \quad (4)$$

where α describes porosity–permeability relationship caused by the loading process, which can be expressed as follows:

$$\frac{k}{k_0} = \left(\frac{\phi}{\phi_0} \right)^\alpha \quad (5)$$

An idealized capillary model is defined at $\alpha = 2$, whereas $\alpha \geq 3$ signifies fractured porous media (Bernabé, 2003; Petunin, 2011).

David et al. (1994) found that $\gamma = 6.6\text{--}18.1 \times 10^{-3} \text{ MPa}^{-1}$ for five different sandstones. While the lower values of γ ($2.84\text{--}7.68 \times 10^{-3} \text{ MPa}^{-1}$) for sandstones and much higher values of γ ($16.8\text{--}43.5 \times 10^{-3} \text{ MPa}^{-1}$) for silty-shale were obtained by Dong et al. (2010). For different types of rocks, pore compressibility has a substantial impact on stress-dependent permeability.

By combining Equations (3) and (5), pore compressibility can be expressed as (David, 1994)

$$\beta = -\frac{1}{\phi} \frac{\partial \phi}{\partial p_{\text{eff}}} \quad (6)$$

In our experiment, we set a constant pore pressure and increasing confining pressure, therefore pore compressibility can be expressed as

$$\beta = -\frac{1}{\phi} \frac{\partial \phi}{\partial p_c} \quad (7)$$

Table 1
Mineralogy and TOC content for shale samples.

Sample	Quartz (%)	Feldspar (%)	Carbonate (%)	Siderite (%)	Pyrite (%)	Clay (%)	TOC (%)
Y-4	36.3	17.8	11.1	0	3.3	31.5	1.06
L-1	30.8	7.0	31.6	1.4	10.5	18.7	6.69
L-2	37.9	3.8	40	0	2.6	15.7	3.13
L-3	25.4	1.0	56.5	0	6.7	10.4	4.37
L-4	20.3	5.0	27.7	0	1.0	45.5	2.38
L-5	42.4	11.4	10.9	0	1.9	32.9	5.35
L-6	55.4	0	25.4	0	2.0	17.2	3.41
L-7	33.4	12.3	14.1	0	2.6	37.6	5.58

Pore compressibility depends on pore geometry and bulk elastic properties, therefore it is important to investigate various pore compressibility models. Some pore compressibility expressions for different pore geometries are given herein for comparison and analysis.

3.1. Circular pore model

For a circular pore model with inner radius a and outer radius b , the porosity can be represented as $\phi = (a/b)^2$ (Al-Wardy, 2004), and substituted this expression into equation (7). Pore compressibility can be expressed as a function of changing in the inner and outer radius due to a change in confining pressure:

$$\beta = -\left(\frac{2}{a} \frac{\partial a}{\partial p_c} - \frac{2}{b} \frac{\partial b}{\partial p_c}\right) \quad (8)$$

Al-Wardy et al. (2004) derived radial displacement expression of circular pore and showed a change in the inner and outer radii due to a change in the confining pressure

$$\left(\frac{\partial u(a)}{\partial p_c}\right)_{p_p} = \frac{-ab^2}{2(\lambda + \mu)(b^2 - a^2)} - \frac{ab^2}{2\mu(b^2 - a^2)} \quad (9)$$

and

$$\left(\frac{\partial u(b)}{\partial p_c}\right)_{p_p} = \frac{-b^3}{2(\lambda + \mu)(b^2 - a^2)} - \frac{a^2 b}{2\mu(b^2 - a^2)} \quad (10)$$

where both λ and μ are the lamé moduli. Equations (9) and (10) can be substituted into equation (8), therefore we obtained the circular pore compressibility as a function of material elastic parameters

$$\beta = \frac{2(1 + \nu)}{E} \quad (11)$$

where E is the Young's modulus, and ν is the Poisson's ratio. The value of Poisson's ratio has a weak influence on pore compressibility. Hence, for circular pore geometries, pore compressibility depends on the magnitude of Young's modulus.

3.2. Penny-shaped model

David et al. (1994) obtained penny-shaped pore compressibility on the basis of Walsh's (1965) derivation in the case of plane strain as the following expression

$$\beta = \frac{3(1 - 2\nu)}{E} \left[\frac{4}{3\pi} \frac{(1 - \nu^2)}{(1 - 2\nu)\epsilon} - 1 \right] \quad (12)$$

where ϵ is the aspect ratio of the pore. The value of Poisson's ratio still has a weak influence on pore compressibility (Fig. 3b). Pore

compressibility not only depends on the magnitude of Young's modulus, but also the aspect ratio (Fig. 3a). The pore compressibility is sensitive to aspect ratio when it is less than 0.01. The penny-shaped pore compressibility is much higher than circular pore for the same material due to a low value of aspect ratio.

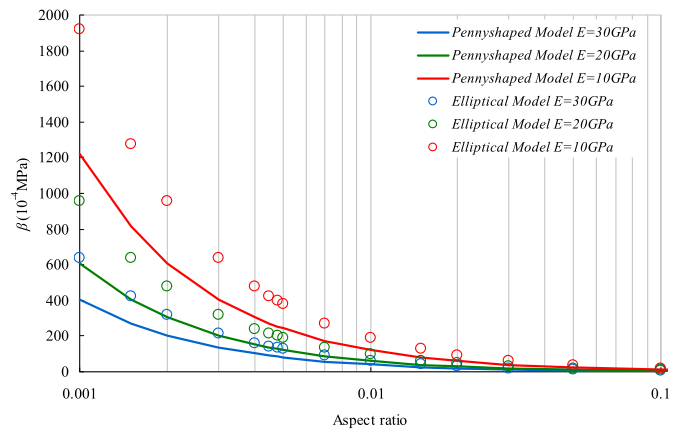
3.3. Elliptical pore model

For the two-dimensional elliptical pore model, the porosity of elliptical pore can be expressed as

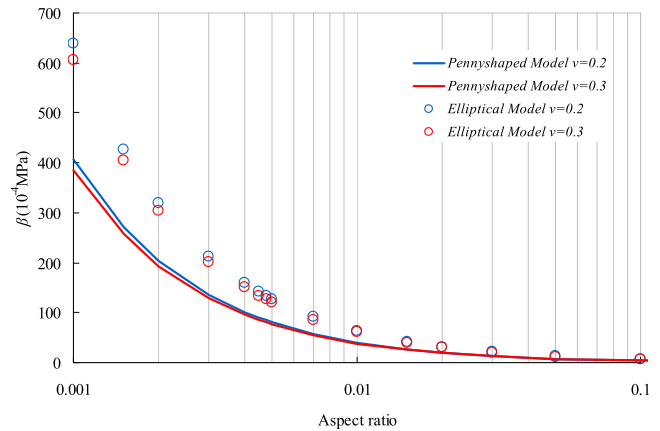
$$\phi = N\pi mn/S \quad (13)$$

where m and n are the half major axis and half minor axis of elliptical pore, respectively. S is cross-sectional area of the hypothetical porous media. N is pore quantity in S . Compared with the change of half major axis, m , and half minor axis, n , with confining pressure, the change of the cross-section area, A , can be considered negligible. Thus equations (7) and (13) can be combined to express the elliptical pore compressibility as

$$\beta = -\left(\frac{1}{m} \frac{dm}{dp_c} + \frac{1}{n} \frac{dn}{dp_c}\right) \quad (14)$$



(a)



(b)

Fig. 3. The semi-log plot of pore compressibility with different models (a) pore compressibility is very high and sensitive with different models and Young's modulus when aspect ratio below 0.01 (b) pore compressibility is insensitive with Poisson's ratio.

Bernabé (1986) presented partial derivative expressions of m and n with respect to the confining pressure p_c as

$$\frac{\partial m}{\partial p_c} = -\frac{n(1-\nu)}{G} \quad (15)$$

and

$$\frac{\partial n}{\partial p_c} = -\frac{m(1-\nu)}{G} \quad (16)$$

where $G = E/2(1+\nu)$ is the shear modulus. Combining Equations (14) and (16), the elliptical pore compressibility as a function of material elastic parameters and aspect ratio is given by

$$\beta = \frac{2(1-\nu^2)}{E} \left(\varepsilon + \frac{1}{\varepsilon} \right) \quad (17)$$

From Equation (17), we can also see that elliptical pore compressibility is sensitive to the Young's modulus and pore aspect ratio (Fig. 3a).

With the assumed values of the Young's modulus (30 GPa) and Poisson's ratio (0.2), we can obtain pore compressibility of circular pore equal to $0.8 \times 10^{-4} \text{ MPa}^{-1}$, while for the penny-shaped model and elliptical pore model, pore compressibility is $400 \times 10^{-4} \text{ MPa}^{-1}$ to $600 \times 10^{-4} \text{ MPa}^{-1}$ at a very low aspect ratio. Furthermore, pore compressibility incurs a sharper increase with a lower Young's modulus (10 GPa) and insensitive to Poisson's ratio (Fig. 3). By observing the three expressions above, it can be found that each expression consists of material and pore geometry terms. The magnitude of the material term depends on the magnitude of Young's modulus (the impact of Poisson's ratio is negligible). The magnitude of pore geometry term depends on the magnitude of aspect ratio. Therefore, circular pores have a much lower compressibility than penny-shaped and elliptical pores due to its pore geometry (aspect ratio equals to unity). In addition, it is important to note that the model selection is crucial to predict the pore compressibility with decreasing values for the Young's modulus.

4. Results and discussion

Test results indicate that permeability of shale samples dropped dramatically more than an order of magnitude with increasing effective stress. With the curve fitting in Fig. 4, Table 2, the stress sensitive coefficient γ can be determined. The values of γ for our

black shale samples over the range of $50.6\text{--}123 \times 10^{-3} \text{ MPa}^{-1}$, which are more than an order of magnitude higher than sandstones. As such, the permeability of shale samples was more sensitive to the effective stress than sandstones.

The porosity sensitivity exponent fitting (Fig. 5, Table 2) show that shale samples have lower porosity sensitivity exponent (1.68–4.9) than sandstones (10–25) (David, 1994; Bernabé, 2003; Yale, 1985) and carbonates (14–128) (Petunin, 2011). This result indicates that the impact of decreasing porosity on permeability of shale is less than sandstones and carbonates. Furthermore, it can be speculated that the proportion of non-effective porosity of shale samples is less than sandstones and carbonates. In other words, compared to fractures, matrix pores in sandstones and carbonates contribute little to permeability. In addition, the porosity sensitivity exponents of L-2 to L-7 yielded values very close to 2.

The fitting (Fig. 6, Table 3) shows that pore compressibility of shale samples were one to two orders of magnitude higher ($194\text{--}503 \times 10^{-4} \text{ MPa}^{-1}$) than sandstone data from literature review (Table 3). This difference indicates that the porosity decrease in shale is more dramatic than in sandstones. Consequently, it can be speculated that the nanopores in shale has a very low aspect ratio compared to that in sandstones. Further, Young's modulus in shale usually is lower than sandstones due to its clay and organic rich (Table 1) composition. In other words, high pore compressibility is the primary reason why the shale permeability exhibits more sensitivity to effective stress.

4.1. Nanopore structure

The mercury intrusion/extrusion capillary pressure curves of selected four samples are shown in Fig. 7, and the incremental Hg injection plot corresponding to a minimum pore diameter of 7.2 nm is shown in Fig. 8. Dominant mesopores and negligible fractures make up the pore volume of sample L-2 and L-3 (Figs. 7 and 8). By contrast, the porosity sensitivity exponents of L-1 and Y-4 were greater than 3, because considerable permeability-controlling microfractures exist in these two samples (Fig. 8).

As shown in Fig. 8, sample L-1 shows a peak in macropore, which indicates the presence of substantial amounts of micron fractures. Nevertheless, even if injection pressure reaches 200 MPa, maximum mercury saturation is still below 70% for L-1 (Fig. 7). Compared with permeability contribution of micron fractures, the permeability contribution of nanopores in L-1 can be negligible ($\phi < 1\%$). Therefore L-1 can be treated as fractured porous media.

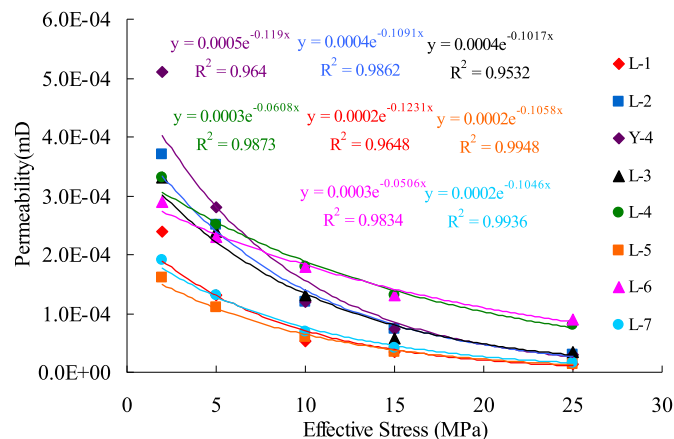


Fig. 4. Exponential curve fit for permeability at varying effective stress for shale samples.

Table 2

Parameters fitting results of porosity-permeability measurements.

Sample	k_0 (mD)	ϕ_0 (%)	γ (10^{-3} MPa^{-1})	α	β (10^{-4} MPa^{-1})
			$k = k_0 e^{-\gamma p}$	$k = k_0 (\phi/\phi_0)^\alpha$	$\phi = \phi_0 e^{-\beta p}$
Y-4	0.00051	2.57	119	4.9	211
			$R^2 = 0.964$	$R^2 = 0.9662$	$R^2 = 0.8915$
L-1	0.00024	0.13	123	3.19	389
			$R^2 = 0.9648$	$R^2 = 0.9681$	$R^2 = 0.9785$
L-2	0.00037	4.28	109	2.375	482
			$R^2 = 0.9862$	$R^2 = 0.989$	$R^2 = 0.9987$
L-3	0.00033	5.58	102	1.6821	444
			$R^2 = 0.9532$	$R^2 = 0.8614$	$R^2 = 0.792$
L-4	0.00033	5.31	60.8	2.2109	284
			$R^2 = 0.9873$	$R^2 = 0.995$	$R^2 = 0.9929$
L-5	0.00016	3.3	105.8	2.031	503
			$R^2 = 0.9948$	$R^2 = 0.9961$	$R^2 = 0.9852$
L-6	0.00029	2.8	50.6	2.5551	194
			$R^2 = 0.9834$	$R^2 = 0.9521$	$R^2 = 0.9237$
L-7	0.00019	2.69	104.6	1.9798	498
			$R^2 = 0.9936$	$R^2 = 0.9887$	$R^2 = 0.98$

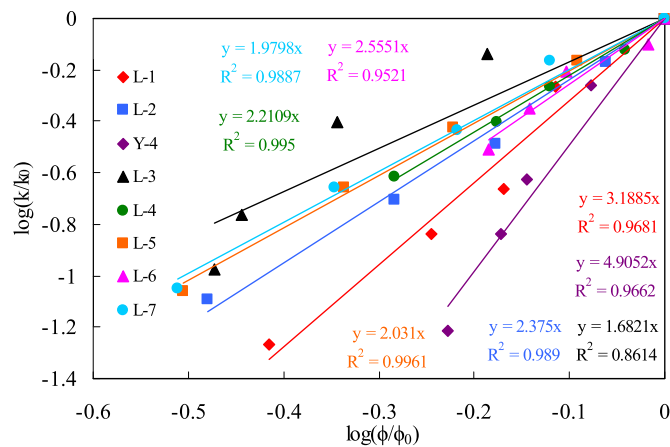


Fig. 5. Permeability–porosity relationship under various effective stress.

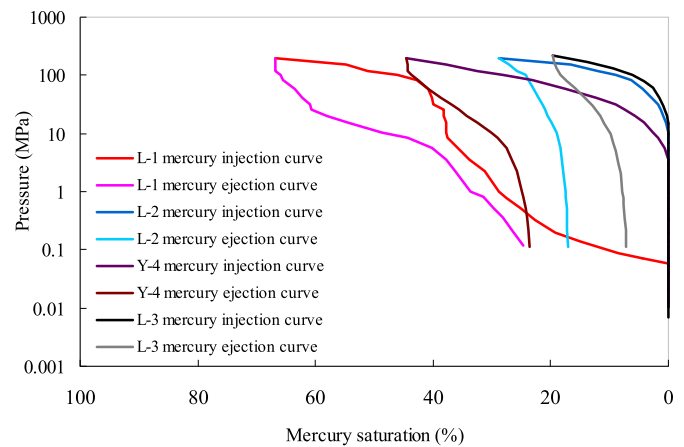


Fig. 7. Mercury intrusion/extrusion capillary pressure curves.

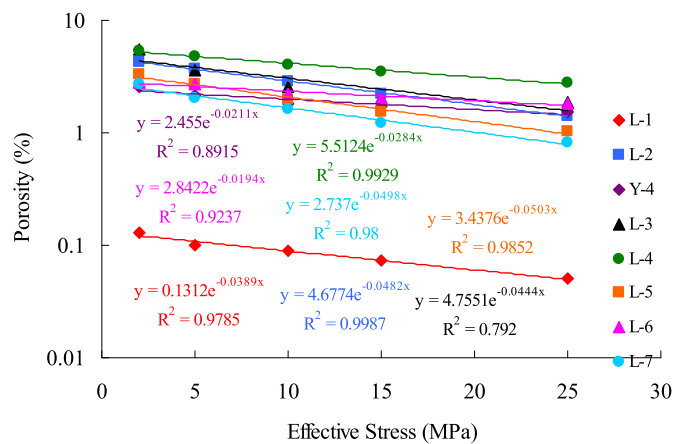


Fig. 6. Pore compressibility fit for shale samples.

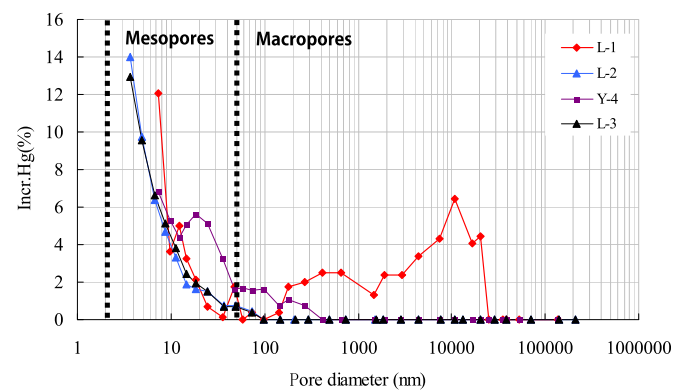


Fig. 8. Incremental Hg injection plot for shale samples.

Table 3

Pore compressibility obtained by fits to experimental data and literatures.

Researcher	Name	Lithologic	Pore compressibility/ 10^{-4}MPa^{-1}
This paper	Longmaxi (Y-4)	Black shale	211
	Longmaxi (L-1)		389
	Longmaxi (L-2)		482
	Longmaxi (L-3)		444
	Longmaxi (L-4)		284
	Longmaxi (L-5)		503
	Longmaxi (L-6)		194
	Longmaxi (L-7)		498
McKee et al. (1988).	Barre Granite	Granite	88
	Bolivar		208
	Appalachian		2610
	San Juan		1943
	Piceance		2610
David et al. (1994).	Piceance	Sandstone	1125
	Adamswiller		4.96
	Fontainebleau		4.88
	Berea		6.73
	Rothbach		9.95
Dong et al. (2010).	Boise	Sandstone	14.39
	Taiwan Chelungpu fault		9.1
			15.8
			10.3
Zhang et al. (2004).	China Ordos	Sandstone	14–21
Li et al. (2006).	—	Sandstone	13–24

The porosity sensitivity exponent of L-1 is very close to 3, thus supporting this conclusion. However, the maximum mercury saturation of other three samples is below 50% where the mean mesopore mercury injection was 93%. Further, there is no peak for all the three samples in macropore and mesopore areas, which indicates that there were small micron and submicron fractures, but abundant micropores in the shale matrix. In other words, nanopores contributed to the permeability of these three samples. Hence it is essential to investigate the impact of nanopore structure on stress-dependent permeability.

The nitrogen adsorption method was used to characterize the pore size distribution of potential abundant nanopores. The nitrogen adsorption–desorption isotherms of the shale samples are shown in Fig. 9. According to the classification of International Union of Pure and Applied Chemistry (IUPAC), N_2 adsorption isotherms of shale samples are classified as the Type IV (Yang et al., 2014). When the relative pressure exceeds 0.45, the envelope of adsorption–desorption isotherms forms the hysteresis loop. All of the eight samples exhibit a narrow hysteresis loop that belongs to the type H3, which corresponds to slit-shaped pores. Slit-shaped pores are beneficial for gas flow and can be easily compressed. Pore size distribution (PSD) was calculated by the BJH (Barett–Joyner–Halenda) method using the desorption isotherm (Fig. 10). Samples with Type H3 hysteresis loop have definite peaks in 3–5 nm in pore size distribution curves, which indicates that the width of slit-shaped pores is 3–5 nm. Such small width may have caused very low aspect ratios (Fig. 11a, b, c). The distribution frequency of slit-shaped pores in samples L-2, L-3, L-5 and L-7 are

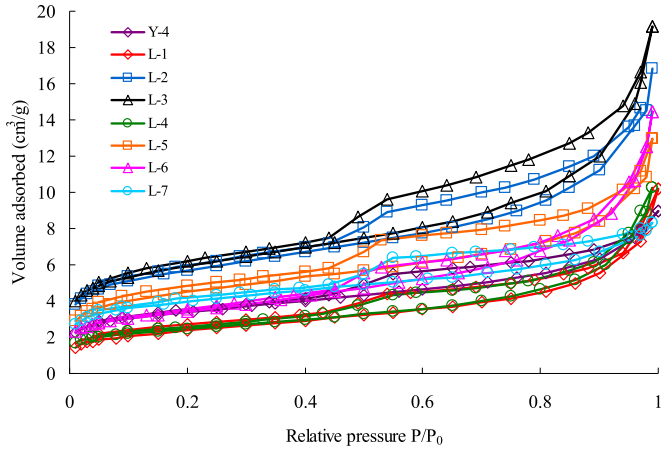


Fig. 9. Nitrogen adsorption-desorption isotherms of shale samples.

higher than others, and therefore have a relatively higher pore compressibility (Table 3).

4.2. Elastic properties

Mechanical properties of shale strongly depend on clay and TOC content (Aoudia, 2010; Kumar, 2012; Alqahtani, 2013). Uniaxial compression tests were conducted to measure elastic parameters of shale samples. The Young's modulus and Poisson's ratio of the samples are shown in Table 4.

Kumar et al. (2012) reported that organic matter in shales is the softer components (5–10 GPa) by nano-indentation measurement, and the elastic modulus decrease with increasing TOC. This result implied that organic matter had a significant influence on rock mechanical properties (Fig. 11d). Normally, the TOC content of the coal ranges between 70% and 90% (Krooss, 2002; Gensterblum, 2010). Therefore the pore compressibility of coal is much higher than shale and other rocks (Table 3). Our results show that Young's modulus for L-1, L-3, L-5 and L-7 were less than 20 GPa with high TOC and clay content.

Clay content of L-1 and L-2 consist of illite, and the clay content of L-3 is montmorillonite-illite mixed layer (Fig. 11a, b). Clay content of Y-4, L-5 and L-7 consists of illite, montmorillonite-illite mixed layer and a small quantity of chlorite. Clay content of L-4 and L-6 consists of illite and chlorite. Table 4 shows the clay content for all samples. Previous studies (Aoudia, 2010; Kumar, 2012; Alqahtani, 2013) show that clay minerals have a substantial impact on mechanical properties. The S-wave velocity of illite is

2.54 km/s (Mavko, 2009), which corresponds to a Young's modulus of 43.88 GPa (Diao, 2013), whereas the S-wave velocity of montmorillonite-illite mixed layer is 1.85 km/s (Mavko, 2009). Thus, it can be reasonably assumed that the Young's modulus of montmorillonite-illite mixed layer is less than 20 GPa. Given the weakness of montmorillonite (Josh, 2012), shale contain a montmorillonite-illite mixed layer are more likely exhibit a low Young's modulus. It should be noted that Young's modulus of Y-4 exceeds 20 GPa, which is likely due to its relative high quartz content. As a hard material, quartz scattered in shale matrix enhances the mechanical properties (Fig. 11e). Samples with quartz content exceed 35% have relative high Young's modulus that is greater than 24 GPa.

The TOC, total clay content and porosity were assumed as soft components which have a negative impact on Young's modulus in a shale matrix (Kumar et al., 2012), and an empirical correlation of soft component volume was presented as follow

$$V_{\text{soft}}(\text{vol}\%) = 2 \times \text{TOC} + \text{total clay content} + \text{porosity} \quad (18)$$

Following Equation (18), the Young's modulus versus soft component volume of our samples are plotted in Fig 12a, which shows scattered data and no discernable trends. However, a good correlation can be observed if the total clay content is replaced by the montmorillonite-illite mixed layer content (Fig. 12b)

$$V_{\text{softm}}(\text{vol}\%) = 2 \times \text{TOC} + \text{montmorillonite} \\ - \text{illite mixed layer content} + \text{porosity} \quad (19)$$

Fig. 12b illustrates that montmorillonite-illite mixed layer content, rather than total clay content, has a substantial impact on the Young's modulus of our shale samples.

Conventional triaxial tests with increasingly effective confining pressure were conducted on shale samples (Fig. 13). According to the idealized stress-strain curves schematic illustration of rock mechanical constitutive laws (Zoback, 2007), our samples exhibited two behaviors, elastic (quasielastic) and viscoelastic. A typical quasielastic curve is shown with Sample L-2 (Fig. 13a). There is a considerable range in a linearly elastic stage before the failure point is reached in two samples. The extent of elastic stage in L-2 is greater than L-3, which may be a result of the kerogen and clay content (Mokhtari, 2013). Young's modulus is almost unchanged with increasing confining stress.

Pore compressibility increases with decreasing Young's modulus at a constant aspect ratio (Fig. 3). Therefore sample L-1 and L-3 had a relative high pore compressibility (Table 3). However, sample L-2 shows aberrant behavior, highest pore compressibility corresponding to largest Young's modulus. This is due to when Young's modulus exceeds 20 GPa, pore compressibility is sensitive to aspect ratio, yet somewhat sensitive to Young's modulus (Fig. 3). Sample L-2 may have lowest mean width of slit-nanopores (highest micropore distribution below 3 nm), which induced lowest pore aspect ratio and highest pore compressibility.

4.3. Fracture scale

Walsh (1981) derived a fracture model that describes the stress-dependent permeability as follows

$$k/k_0 = \left[1 - \sqrt{2}(h/a_0)\ln(P/P_0) \right]^3 \left[\frac{1 - c(P - P_0)}{1 + c(P - P_0)} \right] \quad (20)$$

The first term of the right side equation was referred as "aperture" term, and the second term is the "tortuosity" term. Bernabé (1986) also gave another expression as follows:

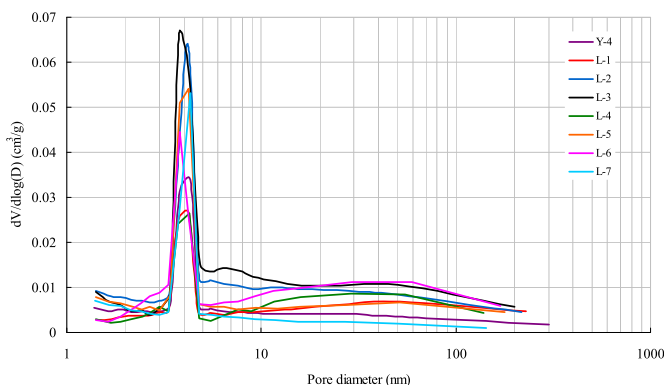


Fig. 10. Pore size distribution of shales from nitrogen desorption.

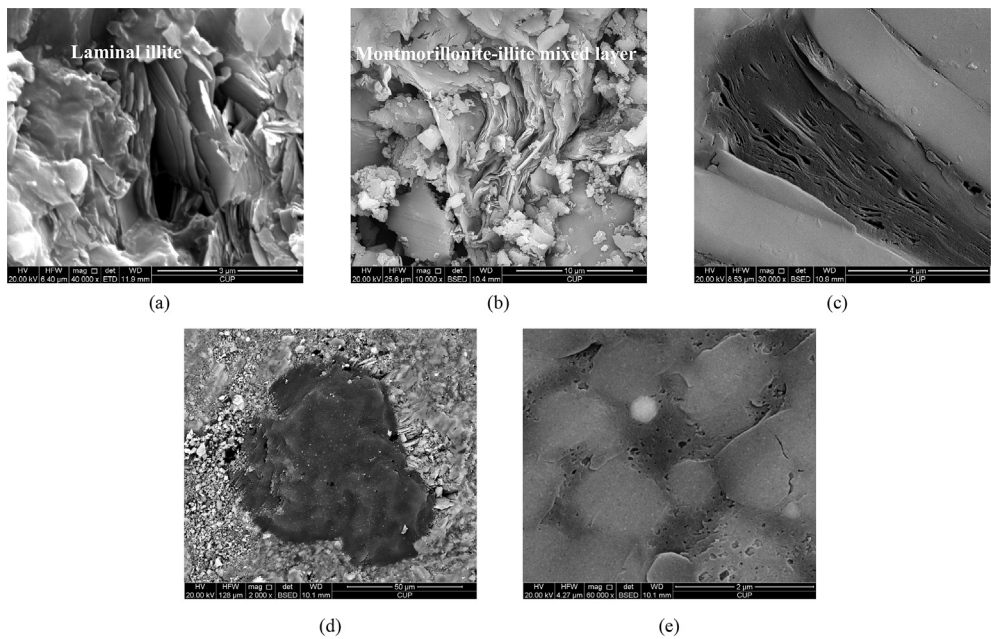


Fig. 11. SEM images of minerals in shale samples (a) laminar illite of sample L-2 (b) montmorillonite-illite mixed layer of sample L-3 (c) montmorillonite-illite mixed layer associated with organic matters (d) organic matters embed in matrix (e) scattered quartz grains in matrix.

Table 4
Statics mechanical properties for shale samples.

Sample	Lithologic	Young's modulus (GPa)	Poisson's ratio	Montmorillonite-illite mixed layer (%)	Illite (%)	Chlorite (%)
Y-4	Black siliceous shale	24	0.26	18	9.45	4.05
L-1		18	0.29	0	18.7	0
L-2		30	0.27	0	15.7	0
L-3		18	0.33	10.4	0	0
L-4		22	0.26	0	35.035	10.465
L-5		16	0.3	19.411	8.255	5.264
L-6		28	0.24	0	16.168	1.032
L-7		12	0.31	21.808	9.776	6.016

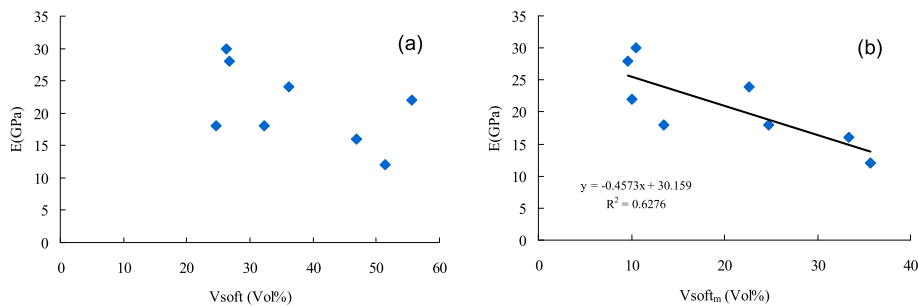


Fig. 12. Relationship between soft volume components and Young's modulus of shale samples (a) soft component volume consist of TOC, total clay content and porosity; (b) soft component volume consist of TOC, montmorillonite-illite mixed layer and porosity.

$$\left(\frac{k}{k_0}\right)^{\frac{1}{c}} = A \ln\left(\frac{P}{P_0}\right) + B \tag{21}$$

Walsh et al. (1984) pointed out that the exponent on the left side of Equation (21) is typically found as being equal to less than one-third ($n > 3$) in measurement results. This exponent is equal 1/3 only if $c = 0$, which indicates that fracture contact area is constant with low pressure. Then Equations (20) and (21) can be written as:

$$\left(\frac{k}{k_0}\right)^{\frac{1}{3}} = 1 - \left(\frac{\sqrt{2}h}{a_0}\right) \ln\left(\frac{P}{P_0}\right) \tag{22}$$

where h is the root-mean-square value of the fracture height distribution relative to roughness, and a_0 is half-aperture at reference pressure. The fracture roughness can be quantitatively estimated by semilog curve fitting as in Fig. 14.

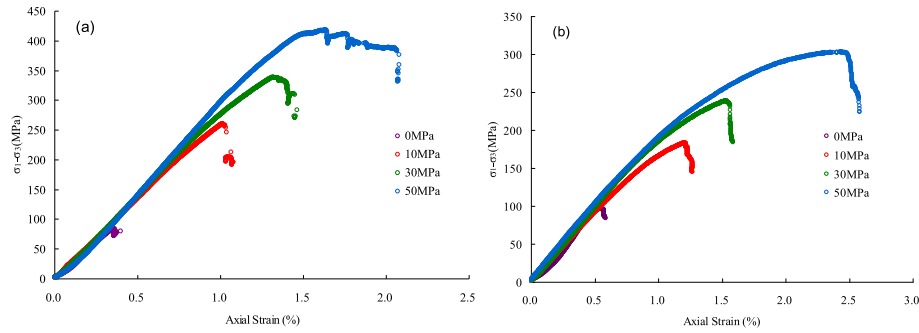


Fig. 13. Stress-Strain curves for triaxial test (a) Sample L-2 showed elastic behavior (b) Sample L-3 showed viscoelastic behavior.

As shown in Figs. 14, L-1 and Y-4 show linear relationship by using the Walsh model over the range of applied pressures. The average slope $\sqrt{2}h/a_0$ equal to 0.566, which is a factor of two greater than the artificial fractures formed with Ottawa sand proppant in the Barnett shale (0.22) (Kassis, 2010). The steep slope is induced by high roughness and small aperture. Therefore, the micron-to submicron scale fractures (Fig. 8) in L-1 and Y-4 and the sub-millimeter scale proppant fractures have different slopes. The permeability of the sample with small fracture apertures is more sensitive to the effective stress than the samples with large fracture apertures. Hence, microfracture permeability is more stress sensitive than artificial fracture permeability.

The curves of L-2 to L-7 do not show a good fit with the Walsh model, and appear nonlinear over the range of applied pressures. This is because micron-submicron fractures cannot be found in these cores (Fig. 8). The pore space of L-2 to L-7, inferred from mercury injection curves (Figs. 7 and 8), should be considered as nano-scale elliptical or slit-shaped pores, rather than fractures at the micron-submicron scale. For this reason, if the scale and permeability of the matrix pores can be considered negligible compared to fracture scale and permeability, the Walsh model can be fitted with the stress–permeability relationships. If the fractures are at the nano-scale, the scale and permeability of matrix pores cannot be considered negligible, and the Walsh model cannot be applied.

5. Conclusions

Stress dependent permeability and porosity of shale samples from Sichuan Basin of China were measured. For all the tested shale

samples, regardless of the presence of microfractures, the exponential law can describe the relationship between shale permeability and various effective stress. Shale permeability is more sensitive to effective stress compared to sandstones because shale had much higher pore compressibility than sandstones. Three analytical expressions correspond to different pore geometries indicate low pore aspect ratio and Young's moduli will induce high pore compressibility. MICP, nitrogen adsorption and rock static mechanical tests were conducted to develop a greater understanding about pore structures and mechanical properties. It was found that nano-scale pores accounted for the largest volume. Slit-shaped nanopores, which dominated all of our samples, were identified by the shape of nitrogen adsorption–desorption isotherms. The slit-shaped nanopores with low aspect ratio (less than 0.01) resulted in high pore compressibility. The triaxial tests show that Young's modulus of a given shale sample is almost unchanged with increasing confining stress. Samples with high TOC and montmorillonite-illite mixed layer are more likely have a lower Young's modulus. However, pore compressibility is insensitive to Young's modulus when Young's modulus exceeds 20 GPa, therefore shale samples with low pore aspect ratio still exhibit high pore compressibility with a high Young's modulus. Only if Young's modulus is less than 20 GPa, can the influence pore compressibility be dramatic. Shale drill cores with micron-submicron scale fractures fit the Walsh model and show that permeability of micron-to submicron scale natural fractures are more stress sensitive than artificial produced fractures. Shale drill cores with only nano-scale pores do not fit the Walsh model because slit-shaped, elliptical, and circular pores are all at the nano-scale.

The combination of the experiments and presented pore compressibility models suggested that an exponential explicit form can estimate the permeability and porosity change under effective stress. The slit-shaped and elliptical pore compressibility models can be employed in exponential function. Further, the porosity sensitivity exponent range from two through three for shale matrix. However, considering the fractures in shale matrix, the porosity sensitivity exponent may much greater than three. Hence, the impact of porosity sensitivity exponent on stress-dependent permeability cannot be negligible and need to be further investigated.

Acknowledgments

The authors would like to acknowledge the financial support of the National Natural Science Foundation of China (Grant No. 51274214), Ministry of Education of China through the Science and Technology Research Major Project (Grant No. 311008), Specialized Research Fund for the Doctoral Program of Higher Education of China (20120007110012).

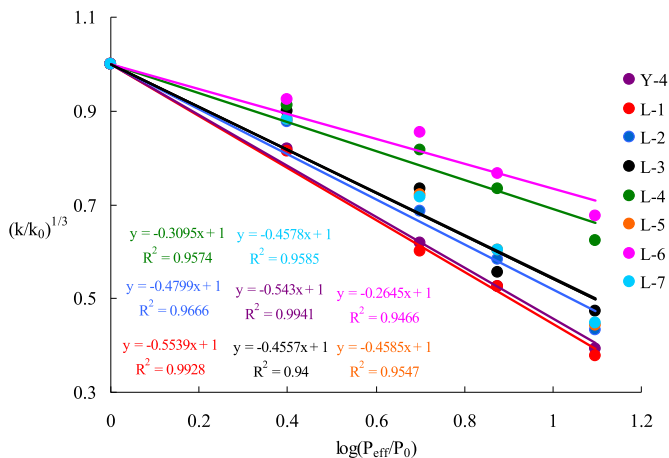


Fig. 14. Curve fitting of Walsh model for shale samples.

Nomenclature

d	pore diameter
θ	contact angle
σ	surface tension
p	applied pressure
p_{eff}	effective stress
p_c	confining pressure
p_p	pore pressure
n_k	permeability effective stress coefficient
β	pore compressibility
a	inner radius of circular pore model
b	outer radius of circular pore model
λ	lamé moduli
μ	shear moduli
S	cross-sectional area of the hypothetical porous media
N	pore quantity in S
k	permeability
k_0	permeability at reference stress
γ	stress sensitivity coefficient
ϕ	porosity
ϕ_0	porosity at reference stress
α	porosity sensitivity exponent
ε	aspect ratio
E	Young's modulus
ν	Poisson's ratio
V_{soft}	soft component volume
V_{softm}	soft component volume for montmorillonite-illite mixed layer
h	r.m.s value of the height distribution of fracture surface
a_0	half aperture of fracture at reference stress
c	change in the ratio of contact area to fracture area with pressure
ω	exponent of measurement results
A, B	constant group

References

- Alqahtani, A.A., Mokhtari, M., Tutuncu, A.N., Sonnenberg, S., 2013, August 12. Effect of Mineralogy and Petrophysical Characteristics on Acoustic and Mechanical Properties of Organic Rich Shale. Society of Petroleum Engineers. <http://dx.doi.org/10.1190/URTEC2013-045>.
- Al-Wardy, W., 2004. Effective stress law for the permeability of clay-rich sandstones. *J. Geophys. Res.* 109 (B4).
- Aoudia, K., Miskimins, J.L., Harris, N.B., Mnich, C.A., 2010, January 1. Statistical Analysis of the Effects of Mineralogy on Rock Mechanical Properties of the Woodford Shale and the Associated Impacts for Hydraulic Fracture Treatment Design. American Rock Mechanics Association.
- Bernabé, Y., 1986. The effective pressure law for permeability in Chelmsford granite and Barre granite. *Int. J. Rock Mech. Min. Sci. Geomechanics Abstr.* Pergamon 23 (3), 267–275.
- Bernabé, Y., Mok, U., Evans, B., 2003. Permeability-porosity relationships in rocks subjected to various evolution processes. *Pure Appl. Geophys.* 160 (5–6), 937–960.
- Berryman, J.G., 1992. Effective stress for transport properties of inhomogeneous porous rock. *J. Geophys. Res. Solid Earth* (1978–2012) 97 (B12), 17409–17424.
- Chalmers, G., Ross, D., Bustin, R., 2012. Geological controls on matrix permeability of Devonian Gas shales in the Horn River and Liard basins, northeastern British Columbia, Canada. *Int. J. Coal Geology* 103, 120–131.
- Cho, Y., Ozkan, E., Apaydin, O.G., 2013, May 1. Pressure-dependent Natural-fracture Permeability in Shale and its Effect on Shale-Gas Well Production. Society of Petroleum Engineers. <http://dx.doi.org/10.2118/159801-PA>.
- Clarkson, C.R., Jensen, J.L., Pedersen, P.K., Freeman, M., 2012. Innovative methods for flow-unit and pore-structure analyses in a tight siltstone and shale gas reservoir. *AAPG Bull.* 96, 355–374.
- Curtis, M.E., Ambrose, R.J., Sondergeld, C.H., 2010, January 1. Structural Characterization of Gas Shales on the Micro- and Nano-scales. Society of Petroleum Engineers. <http://dx.doi.org/10.2118/137693-MS>.
- David, C., Wong, T., Zhu, W., et al., 1994. Laboratory measurement of compaction-induced permeability change in porous rocks: implications for the generation and maintenance of pore pressure excess in the crust. *J. Pageoph.* 143, 425–456.
- Diao, H.Y., 2013. Rock mechanical properties and brittleness evaluation of shale reservoir. *Acta Petrol. Sin.* 09, 3300–3306.
- Dong, J.J., Hsu, J.Y., Wu, W.J., et al., 2010. Stress-dependence of the permeability and porosity of sandstone and shale from TCDP Hole-A. *Int. J. Rock Mech. Min. Sci.* 47 (7), 1141–1157.
- Gangi, A., 1978. Variation of whole and fractured porous rock permeability with confining pressure. *Int. J. Rock Mech. Mining Sci. Geomech. Abstracts* 15 (5), 249–257.
- Gensterblum, Y., et al., 2010. European inter-laboratory comparison of high pressure CO₂ sorption isotherms II: natural coals. *Int. J. Coal Geology* 84 (2), 115–124.
- Ghabezloo, S., et al., 2009. Effective stress law for the permeability of a limestone. *Int. J. Rock Mech. Min. Sci.* 46 (2), 297–306.
- Jones, F.O., 1975. A Laboratory Study of the Effects of Confining Pressure on Fracture Flow and Storage Capacity in Carbonate Rocks. *SPE* 4569.
- Josh, M., Esteban, L., Delle Piane, C., Sarout, J., Dewhurst, D.N., Clennell, M.B., June 2012. Laboratory characterisation of shale properties. *J. Petroleum Sci. Eng.* 88–89, 107–124.
- Kassis, S.M., Sondergeld, C.H., 2010, January 1. Gas Shale Permeability: Effects of Roughness, Proppant, Fracture Offset, and Confining Pressure. Society of Petroleum Engineers. <http://dx.doi.org/10.2118/131376-MS>.
- Krooss, B.M., et al., 2002. High-pressure methane and carbon dioxide adsorption on dry and moisture-equilibrated Pennsylvanian coals. *Int. J. Coal Geology* 51 (2), 69–92.
- Kumar, V., Sondergeld, C.H., Rai, C.S., 2012, January 1. Nano to Macro Mechanical Characterization of Shale. Society of Petroleum Engineers. <http://dx.doi.org/10.2118/159804-MS>.
- Kwon, O., et al., 2001. Permeability of Wilcox shale and its effective pressure law. *J. Geophys. Res.* 106 (B9), 19339–19353.
- Li, M., Qiao, G.A., Chen, H., 2006. Experimental and theoretical study on rock stress-sensitivities in low permeability sandstone. *Drill. Prod. Technol.* 04, 91–93.
- Mavko, G., Mukerji, T., Dvorkin, J., 2009. *The Rock Physics Handbook*. Cambridge University Press.
- McKee, C.R., Bumb, A.C., Koenig, R.A., March 1988. Stress-dependent permeability and porosity of coal and other geologic formations. *SPE Form. Eval.* 81–91.
- Mokhtari, M., Alqahtani, A.A., Tutuncu, A.N., 2013, August 12. Impacts of Stress, Natural and Induced Fractures on Mechanical Properties of Organic-rich Shales. Society of Petroleum Engineers. <http://dx.doi.org/10.1190/URTEC2013-058>.
- Petunin, V.V., Yin, X., Tutuncu, A.N., 2011, January 1. Porosity and Permeability Changes in Sandstones and Carbonates under Stress and Their Correlation to Rock Texture. Society of Petroleum Engineers. <http://dx.doi.org/10.2118/147401-MS>.
- Reyes, L., Osisanya, S.O., 2002. Empirical correlation of effective stress dependent shale rock properties. *J. Can. Petroleum Technol.* 27 (12), 47–53.
- U.S. Energy Information Administration, June, 2013. Technically Recoverable Shale Oil and Shale Gas Resources: an Assessment of 137 Shale Formations in 41 Countries outside the United States.
- Walsh, J.B., 1965. The effect of cracks on the compressibility of rock. *J. Geophys. Res.* 70 (2), 381–389.
- Walsh, J.B., 1981. Effect of pore pressure and confining pressure on fracture permeability. *Int. J. Rock Mech. Min. Sci. Geomechanics Abstr.* 18 (5), 429–435.
- Walsh, J.B., Brace, W.F., 1984. The effect of pressure on porosity and the transport properties of rock. *J. Geophys. Res. Solid Earth* (1978–2012) 89 (B11), 9425–9431.
- Washburn, E.W., 1921. The dynamics of capillary flow. *Phys. Rev.* 17, 273–283.
- Yale, D.P., Nur, A.P., 1985. Network modeling of flow, storage, and deformation in porous rocks. In: 1985 SEG Annual Meeting.
- Yang, F., Ning, Z.F., Liu, H.Q., Jan 2014. Fractal characteristics of shales from a shale gas reservoir in the Sichuan Basin, China. *Fuel* 115, 378–384.
- Zhang, H., Kang, Y.L., Chen, Y.J., et al., 2004. Deformation theory and stress sensitivity of tight sandstones reservoirs. *Nat. Gas. Geosci.* 05, 482–486.
- Zoback, M.D., 2007. *Reservoir Geomechanics*. Cambridge University Press.